Nanoscale Advances

ROYAL SOCIETY OF CHEMISTRY

PAPER

View Article Online
View Journal | View Issue

Cite this: *Nanoscale Adv.*, 2026, **8**, 1906

Amorphous NiFe oxide derived from an air-pyrolyzed Prussian blue analogue with rapid complete reconstruction for enhanced oxygen evolution reaction

Zhen Cao, Wenhui Yan, Haozhe Shi, Tingting Zhou,* Zhifei Sun, Yuhan Yang, Jiali Zhang, Wenbin Zhang and Kaili Wang*

Developing efficient and stable non-precious metal electrocatalysts for the oxygen evolution reaction (OER) is crucial for sustainable hydrogen production *via* electrochemical water splitting. In this work, a facile air-pyrolysis strategy converts a NiFe-Prussian blue analogue (PBA) into an amorphous NiFe oxide catalyst (NiFe-250) with outstanding OER performance. The optimized catalyst exhibits an ultralow overpotential of 255 mV at 10 mA cm^{-2}, a Tafel slope of 39.4 mV dec^{-1}, and excellent long-term stability, significantly outperforming both cyanide vacancy-containing catalysts and crystalline oxide catalysts derived from the same precursor. We demonstrate that the amorphous structure undergoes rapid and complete reconstruction into active NiFeOOH under OER conditions. Furthermore, the direct growth of the catalyst on nickel foam (NiFe-250@NF) results in a further reduced overpotential of 220 mV at 10 mA cm^{-2} and stable operation for over 100 hours, highlighting its practical applicability. This study elucidates the structural evolution of the PBA during air pyrolysis and the OER performance of the resulting catalysts. By unraveling the reconstruction behavior and electrochemical characteristics of the amorphous structure, we reveal the origin of the superior performance, offering a universal strategy for designing high-performance OER electrocatalysts.

Received 22nd September 2025
Accepted 27th January 2026

DOI: 10.1039/d5na00904a

rsc.li/nanoscale-advances

Introduction

In response to growing environmental and energy challenges, numerous research initiatives focused on new energy solutions have been proposed.[1–5] Among them, electrochemical water splitting that can effectively utilize renewable electricity has received widespread attention. The primary advantage of electrochemical water splitting lies in its production of clean and green hydrogen energy. Efficient electrochemical water splitting is considered to provide an effective technological solution for subsequent energy demand.[6–12] However, the oxygen evolution reaction (OER) at the anode of electrochemical water splitting is considered a bottleneck due to its sluggish kinetics, which limits the overall efficiency of the process. The intrinsic hysteresis of the OER has sparked the enthusiasm of many researchers. Many researchers have focused their efforts on developing high-performance OER catalysts.[13–16] With the in-depth development of research, transition metal OER catalysts, which can play a huge role like precious metal catalysts (such as Ru, Ir, RuO_2, and IrO_2), have greatly promoted the development of this field.[17–19] This approach also reduces costs and lays the foundation for future practical applications.

Coordination polymers have always been one of the most effective precursors for preparing transition metal catalysts.[20] Among them, Prussian blue analogues (PBAs), as classic, inexpensive, and easily prepared ordered metal–cyanide (CN) coordination polymers, have shown promising application prospects in the field of electrochemical energy storage and conversion.[21–23] PBAs are also highly attractive for OER applications due to their structural flexibility.[24,25] Firstly, the adjustable range of element components in PBAs is wide and the preparation of PBAs from single element components to high-entropy PBAs is convenient.[26] Secondly, different types of transition metal compounds, such as oxides, chalcogenides, and phosphides, can be obtained through gas-phase or liquid-phase reactions.[27–29] Thirdly, the morphology of PBAs also has tunability, and they can be grown into arrays or prepared into different types of framework or hollow structures.[30,31] In addition, with the deepening of research, the structural evolution and catalytic mechanism of PBAs and their derivatives in the OER have also been further explored.[32,33]

In recent years, defect engineering and structural modulation have become a universal strategy for enhancing catalytic performance.[34–40] This approach is increasingly crucial in the

College of Chemical Engineering and Environmental Chemistry, Weifang University, Weifang 261061, China. E-mail: zhoutt@wfu.edu.cn; 20220043@wfu.edu.cn

field of electrocatalytic oxygen evolution and can also enable PBAs to perform more effectively in the OER.[41–46] Many cutting-edge research studies have further advanced their application in the OER by preparing a PBA with CN vacancies (V_{CN}) through different atmospheres of plasma or pyrolysis in inert gases.[47–50] These research studies provide new perspectives for the future, while also suggesting that PBAs can be regulated in a simpler and more cost-effective way to play a greater role. Here, we prepared an amorphous NiFe oxide for the OER using a simple method of thermal decomposition of NiFe PBA in air. During the process of air pyrolysis, NiFe-PBA undergoes a series of transformations, evolving from a PBA to a PBA with V_{CN}, then to an amorphous oxide, and finally to a crystalline oxide. This amorphous oxide exhibits excellent OER activity, surpassing that of both the PBA containing V_{CN} and the corresponding derived oxides. We have not only developed highly active catalysts but also gained deeper insights into the structural transformations they undergo during the OER. In the OER, the material initially employed acts as a pre-catalyst, undergoing a series of transformations under conditions of high oxidative potential. Demonstrating catalytic activity is fundamentally contingent upon the ability of the pre-catalyst to morph completely into its active phase. This transformation is critical as it directly influences the performance of the catalyst in facilitating the OER process. Through systematic analysis of the reaction products, this study reveals that the amorphous oxide phase prepared using NiFe PBA as a precursor exhibits superior OER performance compared to both the PBA containing V_{CN} catalysts and crystalline oxide catalysts. This enhancement is primarily attributed to its capability to rapidly generate active sites, effectively stabilize elemental components, and achieve complete transformation into the active phase, thereby exposing more accessible active sites. Additionally, due to the good tunability of the method for obtaining amorphous oxides from processing PBA precursors, we further explored its integration with other suitable PBA modulation techniques. Herein, it was fabricated as a direct electrode grown on Ni foam (NF), enabling it to exhibit enhanced OER performance. We also hope that this can be synergistically combined with other excellent methods for handling the PBA, allowing it to play a more significant role in the OER and achieve an outcome where the whole is greater than the sum of its parts.

Results and discussion

PBAs transform into corresponding oxides upon high-temperature heating, exhibiting distinct states at different treatment stages. Additionally, pre-catalysts in different states undergo varied structural transformations during the OER, which is precisely the key reason for the performance differences among catalysts. In this study, NiFe-PBA was treated at different temperatures to obtain derivatives in various states, aiming to explore the optimal calcination temperature in air for maximizing OER performance. To optimize the conditions, a temperature gradient of 50 °C was established. NiFe-PBA derivatives were obtained by calcination at 200 °C, 250 °C, 300 °C, and 350 °C, denoted as NiFe-200, NiFe-250, NiFe-300, and NiFe-350, respectively. The thermogravimetric (TG) analysis of NiFe-PBA reveals some of its variation characteristics at different temperature nodes. And the morphology evolution of NiFe-PBA with temperature can be clearly observed through SEM images. In addition, TG analysis was used to observe the weight loss of NiFe-PBA at different heating temperatures (Fig. 1a). Prior to thermal treatment, the NiFe-PBA precursor is characterized by a smooth nanocube structure (Fig. S1a). Upon heating, the initial change corresponds to the evaporation of adsorbed water, followed by complete removal of crystalline water at approximately 170 °C. As the temperature increases, a slight efflux of CN occurs, and the once-smooth morphology of NiFe-PBA's surface is altered (Fig. S1b). At 250 °C, the coordination between the CN ligands and the metal ions is disrupted, triggering partial degradation. As the temperature escalates to 350 °C, complete oxidation of CN occurs.[51–53] The SEM images (Fig. S1c–e) clearly illustrate these transformations, showing the morphology of the NiFe-PBA precursor becoming increasingly rough and uneven until a nanoporous cube structure is formed (Fig. 1a).

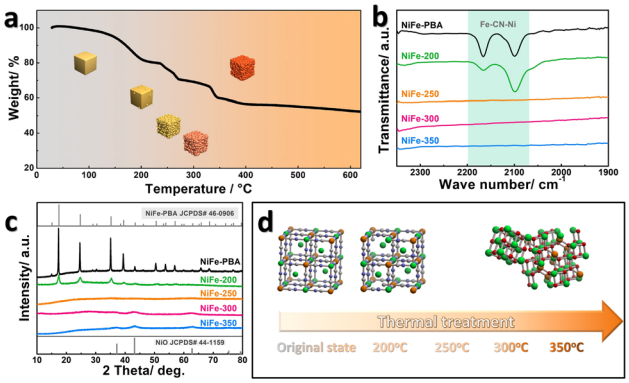

Fig. 1 (a) TGA spectrum of NiFe-PBA and schematic illustration of morphology at different heating temperatures. (b) XRD patterns and (c) FT-IR spectra of the NiFe-PBA at different heating temperatures. (d) Schematic illustration of the material structure.

Changes in the functional groups of the PBA were characterized by Fourier Transform Infrared (FT-IR) spectroscopy (Fig. 1b), confirming its Prussian blue structure. The distinct asymmetric band at 2166 cm^{-1} corresponds to CN vibrations in the Fe^{3+}–C≡N–Ni^{2+} framework, while the band at 2098 cm^{-1} matches the Fe^{2+}–C≡N–Ni^{2+} configuration.[54] Compared to NiFe-PBA, the NiFe-200 derivative exhibits a marked attenuation in the relative intensity of the characteristic 2166 cm^{-1} vibrational band. Given that the CN triple bond possesses high bond energy and is difficult to cleave, this observed weakening must result from the rupture of metal–CN coordination bonds rather than CN bond scission, strongly indicating the formation of V_{CN}. The concomitant reduction in the iron oxidation state further corroborates the V_{CN} generation mechanism, which aligns consistently with previously documented phenomena in analogous systems. Peaks pertaining to CN become non-discernible in NiFe-250, NiFe-300, and NiFe-350 (Fig. 1b), suggesting full decomposition or overflow of CN post 250 °C.

At this point, the changes in functional groups in NiFe-PBA have been elucidated, and the XRD pattern in Fig. 1c shows the evolution of its crystal structure. The crystalline phase of the precursor is a typical PBA structure, which is $Ni_3(Fe(CN)_6)_2 \cdot 10H_2O$ (JCPDS# 46-0906). NiFe-200 retains a crystalline structure similar to the NiFe-PBA precursor, albeit with broader peak widths indicating reduced grain size and enhanced lattice defects. Herein, electron spin resonance (ESR) spectroscopy was employed to further confirm the presence of V_{CN} in NiFe-200 (Fig. S2). A distinct signal at a *g*-factor of 2.03, which is characteristic of electrons trapped at surface V_{CN} sites, is significantly enhanced in NiFe-200 compared to the NiFe-PBA precursor.[50,55] The XRD pattern of NiFe-250 suggests an amorphous phase, while NiFe-300 adopts the crystalline structure of NiO. As the thermal treatment temperature increased to that used for NiFe-350, the intensity of the XRD diffraction peaks significantly enhanced, indicating a further improvement in the material's crystallinity. It is noteworthy that no distinct crystalline phases corresponding to iron-containing compounds were detected in the patterns, suggesting that iron may exist in an ultrafinely dispersed form or as a solid solution within the NiO lattice. To further clarify the state of iron, we increased the calcination temperature to 400 °C for verification. As shown in Fig. S3, the diffraction peaks of NiO in this sample became sharper and their intensity increased markedly, indicating further improved crystallinity and significant grain growth. Additionally, a weak yet discernible diffraction peak was observed at $2\theta \approx 35.6°$, which can be attributed to the [311] crystal plane of $NiFe_2O_4$. This phenomenon, where crystallinity continuously enhances and new crystalline phases gradually emerge with increasing temperature, is consistent with the evolutionary trends reported in the previous studies.[56,57] Synthesizing insights from the FT-IR spectra, NiFe-250 might adopt an oxide state akin to others, given undetectable evidence of metal-coordinated CN. It is noteworthy that no V_{CN} signal was detected in the ESR test (Fig. S2), ruling out the possibility of NiFe-250 being a PBA with V_{CN}. This result indicates that it is most likely an amorphous oxide formed by the oxidation of the precursor in air. Overall, the thermal treatment of NiFe-PBA in air follows a clear transformation pathway: initial formation of CN vacancies, followed by conversion to oxides, with crystallinity improving progressively at higher temperatures (Fig. 1d).

TEM was employed to further investigate the morphology and structure of NiFe-250. Consistent with the SEM image (Fig. S1c), the TEM images reveal that NiFe-250 retains a cubic morphology with an edge length of approximately 70 nm. And the surfaces of these nanocubes are irregular, featuring small particles and rough protrusions (Fig. 2a and b). While FT-IR spectra and XRD patterns provided certain structural information about NiFe-250, high-resolution TEM (HR-TEM) was additionally employed for further analysis. As shown in Fig. 2c, the NiFe-250 nanocubes lack distinct long-range lattice fringes, exhibiting a disordered arrangement that aligns with the amorphous structure indicated by XRD. Furthermore, elemental mapping analysis confirms the homogeneous distribution of Ni, Fe, and O elements throughout the NiFe-250 structure.

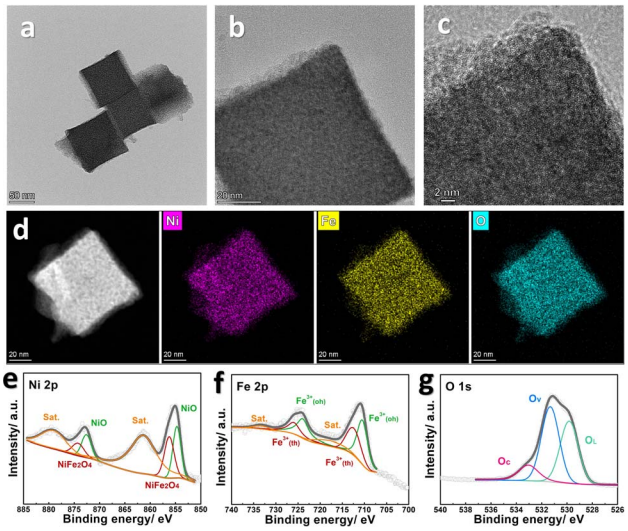

Fig. 2 (a) Low-magnification, (b) high-magnification and (c) high-resolution TEM images of NiFe-250. (d) HAADF-TEM and corresponding elemental mapping of NiFe-250. High-resolution (e) Ni 2p, (f) Fe 2p and (g) O 1s XPS spectra of NiFe-250.

To gain deeper insights into the surface chemical states of the material post-thermal treatment, X-ray Photoelectron Spectroscopy (XPS) data for NiFe-250 are indispensable (Fig. 2e–g and S4). The Ni 2p spectrum of NiFe-250 exhibits typical splitting peaks, which are the representative NiO, $NiFe_2O_4$ and satellite peaks. The splitting peak of 854.73 and 872.56 eV should be attributed to NiO and peaks at 856.23 and 874.23 eV should be attributed to $NiFe_2O_4$, respectively.[58,59] The other peaks correspond to the satellite peaks of Ni. In addition, the XPS spectrum of Fe is also clear. There are different sites for Fe^{3+} in the inverse spinel structure, including tetrahedral (th) sites with high binding energy and octahedral (oh) sites with low binding energy. The peaks at 710.45 and 723.91 eV are attributed to Fe^{3+} oh sites and peaks at 712.46 and 725.92 eV are attributed to Fe^{3+} th sites, respectively. The peaks at 717.65 and 733.26 eV belong to satellite peaks.[60] Besides, the XPS spectrum of the O 1s orbitals is also revealed. The spectrum can be divided into peaks at binding energies of 529.82, 531.32 and 533.05 eV corresponding to lattice oxygen (O_L), vacancy oxygen (O_v) and adsorbed oxygen (O_c), respectively.[61] The weak peak at around 401 eV in the N 1s XPS spectrum may correspond to a small amount of nitrogen oxide adsorbed after CN decomposition (Fig. S4).

From the XPS spectrum combined with the XRD and HR-TEM data, it can be inferred that NiFe-250 is an amorphous oxide in which Ni and Fe are homogeneously mixed. To further investigate the chemical state of NiFe-250, we performed additional characterization using Raman spectroscopy, which is highly sensitive to local coordination environments. As shown in Fig. S5, the vibrational modes observed at 310, 465, and 676 cm^{-1} can be assigned to $NiFe_2O_4$,[56,62] while the mode at 550 cm^{-1} is attributed to NiO.[63] These results provide further confirmation that NiFe-250 consists of a mixture of oxides with poor crystallinity.

In addition, XPS was used to further test and analyze the surface chemical states of other comparative materials (Fig. S6–S9). Notably, NiFe-PBA exhibits distinct characteristics of a Prussian blue analogue. Furthermore, NiFe-200 confirms the FT-IR findings, having transformed into a PBA interlaced with V_{CN} upon heating. In contrast, NiFe-300 and NiFe-350 are identified as oxides, with their predominant phases being NiO and $NiFe_2O_4$, respectively. A clear evolutionary trend can be observed from NiFe-PBA to NiFe-350. First, the chemical states of Ni and Fe undergo significant changes. The NiFe-PBA precursor displays obvious mixed valence states of Ni^{2+}/Ni^{3+} and Fe^{2+}/Fe^{3+}. When the heat treatment temperature increases to 200 °C, the valence states of Ni and Fe change markedly. The proportion of Ni^{3+} decreases significantly, while Fe shows significant Fe^{2+} signals. However, the Fe^{3+} peaks exhibit higher binding energies compared to those in NiFe-PBA. Additionally, the emergence of Fe satellite peaks indicates the formation of some iron oxides, which also aligns with the reason for the higher binding energy. Concurrently, notable changes occur in N species. The originally relatively pure CN groups give way to the appearance of some oxygen-containing species. Combined with the ESR results, it can be inferred that V_{CN} likely form at this stage. The generation of V_{CN} and the presence of partial Fe oxides lead to electron donation and rearrangement between Ni and Fe.[54,64–66] When the temperature increases to 250 °C and above, the distinct CN groups present in NiFe-PBA and NiFe-200 completely disappear in the samples, confirming the thermal decomposition of CN ligands. At this point, Ni and Fe gradually exhibit oxide characteristics. Finally, the evolution of O species indicates progressively deepening oxidation. As the temperature increases from 200 °C to 350 °C, the proportion of lattice oxygen bonded to metals increases, while the O_V proportion correspondingly decreases.[60,61,67] These XPS results, together with the FT-IR and XRD results, collectively outline a complete transformation pathway. When NiFe-PBA is heated in air, CN coordination bonds first break to form V_{CN}, followed by gradual oxidation of metal sites, ultimately forming metal oxides with continuously improving crystallinity.

After understanding the chemical state of the material, its OER performance was subsequently tested. Fig. 3a shows the linear sweep voltammetry (LSV) curves of all samples. From these curves, it can be observed that their electrochemical activity exhibits a certain regularity. The OER activity of the NiFe-PBA derivatives initially increases and then decreases with the treatment temperature. Notably, NiFe-250 demonstrates the most outstanding activity. Furthermore, it is worth noting that the excellent activity of these samples even surpasses that of the precious metal catalyst Ir, as illustrated in Fig. S10a. The performance of all samples is graphically presented in Fig. 3d. Among them, NiFe-250 exhibits the most exceptional activity, with an onset overpotential of 190 mV. When its current density reaches 10 mA cm^{-2} and 50 mA cm^{-2}, the overpotentials are only 255 mV and 310 mV, respectively. Furthermore, it achieves the highest electrochemically active surface area (ECSA) (Fig. S12), indicating a greater abundance of accessible active sites contributing to its enhanced performance. As shown in Fig. 3b, NiFe-250 shows the lowest Tafel slope of 39.4 mV dec^{-1}, which also shows a decreasing and increasing pattern compared to other NiFe-PBA derivative samples. Also, it is lower than the Tafel slope of the precious metal catalyst Ir (Fig. S10b). As shown in Fig. 3c, the Nyquist plot shows that NiFe-250 has the lowest reaction resistance among all samples. Furthermore, to gain deeper insight into the electrochemical behavior, the Nyquist plots were fitted using an equivalent circuit model (Fig. S11, inset), which primarily consists of three components: the solution resistance (R_s), the charge transfer resistance (R_{ct}), and a constant phase resistance. The intercept on the real axis in the high-frequency region corresponds to R_s, while the diameter of the semicircle reflects the magnitude of R_{ct} (Fig. S11). The fitted R_{ct} and R_s values are summarized in Table S1. Notably, NiFe-250 exhibits the smallest R_{ct} value (4.988 Ω cm^{-2}), indicating the most efficient charge transfer kinetics. This result further corroborates its significantly enhanced catalytic performance from an electrochemical dynamics perspective.

After 60 hours of the OER at an overpotential of 270 mV, the current density of NiFe-250 remained stable at 30 mA cm^{-2}, indicating its considerable stability (Fig. 3e). After that, in order to further develop the OER performance of NiFe, NF with high conductivity was introduced as the catalyst electrode carrier. Although the carrier was converted, NiFe-250 still demonstrated excellent OER performance. NiFe-250/NF showed the lowest overpotential, Tafel slope, and reaction resistance among all samples (Fig. S13 and S14 and Table S2). Due to the high conductivity and high liquid flux of NF, NiFe-250/NF exhibits more prominent current density values at high potentials.

Through electrochemical testing, it became evident that the product obtained by simply treating NiFe PBA in air at 250 °C shows excellent OER performance. The superior activity of NiFe-250 compared to the pristine PBA and other derivatives remains unclear. However, it cannot be ignored that the substances generated *in situ* using the catalytic material under the strong oxidation conditions of the OER may be the catalytically active sites.[68] In order to further understand the reasons for the excellent performance, the morphology, structure, and elemental state of NiFe-250 after the OER (NiFe-250-A) were characterized. From SEM and TEM images (Fig. 4a–c), it can be

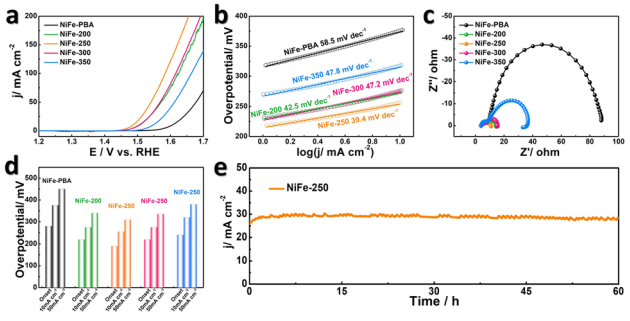

Fig. 3 (a) LSV, (b) Tafel slopes, (c) Nyquist plots and (d) overpotential data bar chart of NiFe-PBA, NiFe-200, NiFe-250, NiFe-300 and NiFe-350. (e) Chronoamperometric tests of NiFe-250 at an overpotential of 300 mV.

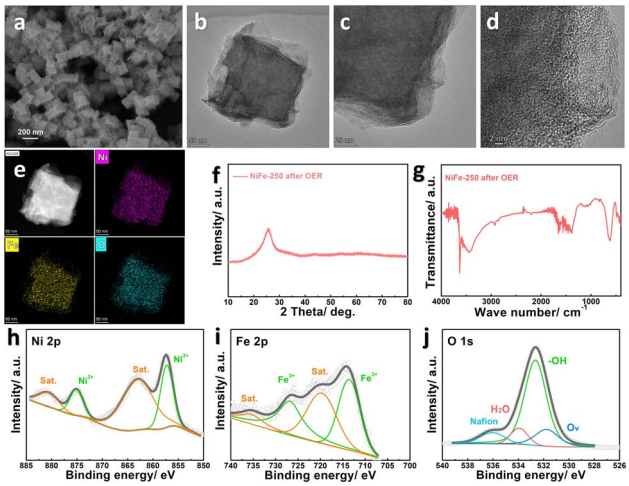

Fig. 4 (a) SEM, (b) low-magnification TEM, (c) high-magnification TEM and (d) high-resolution TEM images of NiFe-250-A. (e) HAADF-TEM and corresponding elemental mapping of NiFe-250-A. (f) XRD pattern and (g) FT-IR spectra of NiFe-250-A. High-resolution (h) Ni 2p, (i) Fe 2p and (j) O 1s XPS spectra of NiFe-250-A.

observed that NiFe-250-A still retains its initial cubic morphology after the OER. The difference is that nanosheets have grown on the surface of these cubes. The change in morphology indicates that the oxidation drive of the OER has indeed disrupted the original state of the catalyst. In addition, HR-TEM was used to observe both the inner cube and the outer nanosheets simultaneously, and no discernible lattice fringes were detected (Fig. 4d). However, similar to NiFe-250, the element distribution of NiFe-250-A remains uniform (Fig. 4e). NiFe-250 was dispersed onto carbon paper and then subjected to the OER. The catalysts after the reaction were systematically characterized using FT-IR, XRD, and XPS techniques. From Fig. 4f, it can be observed that there are no other obvious diffraction patterns observed in NiFe-250-A except for the carbon paper substrate diffraction peaks.

While the XRD and HR-TEM results indicate a lack of a long-range ordered structure in the material, the FT-IR spectrum (Fig. 4g) clearly reveals its fine chemical coordination environment at the short-range scale. Several characteristic vibrational signals attributable to the metal–O–H framework are observed in the spectrum. The broad absorption envelope at around 3450 cm^{-1} arises from the O–H stretching vibrations of adsorbed water and strongly hydrogen-bonded O–H groups, exhibiting spectral features typical of oxyhydroxides. The sharp absorption peak at 3628 cm^{-1} corresponds to the O–H stretching mode of isolated or weakly hydrogen-bonded groups, a signal commonly associated with Ni–O–H.[50] Notably, the absorption peak near 635 cm^{-1} may originate from the coupled response of Fe–O stretching vibrations in FeOOH and Ni–O–H bending vibrations.[50,69] Additionally, the relatively weak peak at 850 cm^{-1} can be further identified as the out-of-plane bending vibration of Fe–O–H.[50] These features collectively indicate that the post-reaction NiFe-250 possesses a local coordination configuration characteristic of Ni–Fe (oxy)hydroxides. To further clarify the oxidation states of the metal elements and the overall chemical coordination environment, we conducted more in-depth characterization using the XPS spectrum (Fig. 4h–j). From the XPS spectrum, it can be observed that the catalyst undergoes substantial changes after the OER. NiFe-250 is converted from the previous amorphous oxide to the hydroxide of NiFe-250-A. Specifically, the splitting peaks at 857.3 and 875.8 eV should be attributed to Ni^{3+} hydroxide and peaks at 863.0 and 880.7 eV should be attributed to the satellite peaks of Ni, respectively.[64] The peaks at 713.6 and 726.8 eV are attributed to Fe^{3+} hydroxide and peaks at 719.7 and 735.4 eV are attributed to the satellite peaks of Fe, respectively.[64] And the O of NiFe-250-A has three states, H_2O, –OH and O_v, respectively.[64] There are other O from the adsorbed H_2O and added Nafion. It can be determined that the NiFe-250 pre-catalyst exhibits optimal OER performance due to its complete conversion into the active NiFeOOH phase. To verify the findings indicated by XPS, we conducted additional transmission electron microscopy analysis on NiFe-250-A. A representative nanoparticle was selected, and its line-scanning compositional profile was examined to validate the completeness of the transformation. As shown in Fig. S15a and b, the particle retained its structural integrity. Linear compositional analysis was first performed along the central axis traversing the entire particle (Fig. S15c). The results show that the signal intensities of Ni, Fe, and O are highly synchronized and uniformly distributed along the entire scanning path. Given the fundamental difference in stoichiometric ratios between metals and O in amorphous oxides and their oxyhydroxides, this homogeneous composition throughout the particle interior directly confirms that the reconstruction proceeds thoroughly from the exterior to the core. To further strengthen this conclusion, supplementary line-scanning analysis was conducted in the edge region of the particle (Fig. S15d), the results of which are fully consistent with those of the central-axis analysis. Together, these data demonstrate that the reconstruction ultimately yields a homogeneous active phase at the bulk scale, rather than merely a thick surface shell. This finding corroborates the chemical state analysis obtained from XPS. This observation is consistent with the outstanding OER activity of V_{CN}-containing NiFe-200, where the presence of V_{CN} in the PBA framework facilitates the formation of the catalytically active NiFeOOH phase under OER conditions.[50] Similarly, oxide catalysts also undergo surface reconstruction during the OER to form active oxyhydroxide layers that enhance their performance.[70] Therefore, the superior OER activity of PBA-derived catalysts can be attributed to the *in situ* generation of NiFeOOH during electrocatalysis.

XPS analysis confirms that the reconstructed NiFe-250 primarily exists in the form of an amorphous NiFeOOH phase. It is particularly important to note that the highly disordered nature of this amorphous structure generates abundant edge sites and structural defects, which are considered key structural features responsible for its excellent OER performance. Current research generally tends to support the view that Fe sites located at edges or defects serve as the primary active centers for the OER, capable of forming highly reactive Fe^{4+}=O intermediates. Meanwhile, the NiOOH matrix in the

catalyst primarily functions as a conductive scaffold that effectively optimizes the oxidation potential of Fe active sites while stabilizing high-valence states, thereby significantly reducing the reaction overpotential.[71–73] It is worth noting that different perspectives still exist regarding the mechanism of catalytically active sites in the NiFeOOH phase. Some studies emphasize that the substitution of Ni by Fe produces a significant electron-withdrawing effect, promoting the generation of high-valence Ni species at lower potentials, and these high-valence Ni species play a crucial role in OER catalytic activity.[74,75] Additionally, other research proposes a synergistic catalytic mechanism between Fe and Ni, where Fe sites are primarily responsible for stabilizing oxygen-radical intermediates, while Ni sites effectively facilitate the formation of O–O bonds.[76] Despite these mechanistic controversies, the academic consensus maintains that both Ni and Fe are indispensable components in the NiFeOOH catalytic system for achieving high oxygen evolution reaction activity.

Notably, NiFe-250 demonstrates superior activity compared to both the V_{CN}-containing sample and crystalline oxide materials. We further performed detailed CV analysis for each pre-catalyst across multiple cycles to investigate this phenomenon. As a pre-catalyst, the amorphous state of NiFe-250 can be completely transformed. Furthermore, it must be emphasized that the reconstruction of NiFe-250 is very rapid, and its CV curve reaches a stable state after the 2nd cycle (Fig. S16c). Rapid reconstruction can not only promptly generate active phases but also effectively prevent Fe leaching. To systematically evaluate the stability of Fe, we employed multiple characterization techniques to compare the Ni/Fe atomic ratios in NiFe-250 and its post-OER counterpart NiFe-250-A, with the data summarized in Table S4. First, the Ni/Fe ratios on the surface and in local micro-areas were calculated based on XPS and EDS data. The results show largely consistent values before and after the reaction, with only a slight decrease in Fe content, indicating that the rapid surface reconstruction effectively suppresses the leaching of Fe species during catalysis. Furthermore, bulk elemental analysis conducted by ICP-OES also demonstrated a stable overall Ni/Fe atomic ratio after the OER test, consistent with the trends observed in XPS and EDS. These consistent findings not only further support that rapid reconstruction mitigates Fe loss, but the agreement between surface and bulk compositions also indirectly reflects a relatively thorough reconstruction process and complete phase transformation into the active species.

In contrast, when NiFe-PBA is directly employed as an OER catalyst, it undergoes anion exchange between $[Fe(CN)_6]^{n-}$ and OH^- in alkaline solution, leading to continuous Fe leaching.[50,77] From Fig. S16a, it can be observed that the redox couples of NiFe-PBA undergo continuous changes during the OER, with the CV curve failing to stabilize completely even after 100 cycles. Ultimately, NiFe PBA will transform into $Ni(OH)_2$ containing trace amounts of Fe during the OER process.[33] By comparison, V_{CN}-containing NiFe-200 achieves rapid stabilization during the OER by limiting Fe loss. In NiFe-200, the removal of CN groups from the PBA framework creates numerous coordinatively unsaturated, open metal sites. Significantly, the exposed Fe centers facilitate the formation of Fe–O bonds during the OER, thereby effectively suppressing iron dissolution into the electrolyte. Finally, under the influence of V_{CN}, an active NiFeOOH surface layer will be formed.[50] The high concentration of V_{CN} significantly accelerates the electrochemical activation kinetics. Consequently, as shown in Fig. S16b, NiFe-200 reaches a stable state as early as the 5th cycle, demonstrating its rapid activation process. Here, by comparing NiFe-PBA and NiFe-200, NiFe-250 can be rapidly reconstructed to avoid Fe loss while fully converted to ensure the utilization of active sites, demonstrating excellent OER performance. Although NiFe-200 can also rapidly establish a stable active phase, its activation exhibits a slight lag compared to amorphous NiFe-250. Compared to NiFe-250, NiFe-300 and NiFe-350 with higher crystallinity exhibit a decrease in performance. When NiFe-300 reaches the second cycle of the CV curve, its redox pair is already stable (Fig. S16d). Notably, NiFe-350 retains nearly identical CV profiles throughout cycling (Fig. S16e), indicating its ability to rapidly form an active surface under OER oxidation conditions. However, the highly crystalline large-grain pre-catalysts undergo surface-limited reconstruction, forming only superficial active components that result in a core–shell architecture. This structural configuration leads to inadequate utilization of internal components during electrocatalysis.[64,78] In contrast, smaller grain dimensions facilitate complete structural reconstruction.[40] The absence of distinct diffraction peaks in the XRD pattern of NiFe-250, combined with the lack of lattice fringes in its HR-TEM images, confirms its amorphous nature and implies the presence of ultra-fine grain dimensions. This structural characteristic facilitates thorough phase transformation, ultimately enhancing the OER performance. In contrast, the grain sizes of NiFe-300 and NiFe-350, calculated from XRD data using the Scherrer equation, are approximately 7.4 and 8.2 nm, respectively. Their relatively larger grain sizes hinder complete reconstruction during the OER process, resulting in only a surface-level transformation into NiFeOOH and a gradual degradation in performance as the grain size increases. Through systematic comparative analysis, it can be determined that the outstanding OER activity of amorphous NiFe-250 stems from its unique dual-phase transformation characteristics. First, it exhibits exceptionally rapid electrochemical activation. Additionally, it undergoes a thorough bulk-phase transformation into active NiFeOOH. This complete reconstruction behavior stands in sharp contrast to that of NiFe-200 with V_{CN} and crystalline NiFe-300 and NiFe-350, ultimately achieving the full utilization of catalytic metal centers.

Based on the comprehensive analysis above, it is concluded that the amorphous pre-catalyst NiFe-250 undergoes rapid and thorough bulk reconstruction under OER conditions and completely transforms into a homogeneous NiFeOOH active phase. The effective retention of Fe during this process preserves the intrinsic catalytic capability of the active sites. Although other samples, including NiFe-200, NiFe-300, and NiFe-350, also achieve electrochemical steady state relatively quickly, the core advantage of NiFe-250 lies in its capability for complete bulk-phase transformation. This unique property enables it to convert the largest population of initial active sites

almost entirely into the largest population of effective NiFeOOH active sites. ECSA measurements directly support this conclusion—NiFe-250 exhibits the highest ECSA value (Fig. S12), indicating the most abundant number of exposed and electrochemically accessible sites among all samples. In contrast, the performance of the other samples is limited by either a lower initial number of active sites or incomplete reconstruction confined to the surface. Both factors lead to a significantly reduced density of utilizable effective active sites. Therefore, the exceptional performance of NiFe-250 stems from the perfect synergy between two critical factors, abundant site exposure and thorough site activation.

The excellent performance of the catalyst after OER drive is attributed to the reasonable construction of the NiFe-250 structure, and it is believed that this reasonable construction has universality. In recent years, the preparation of direct electrodes has been a hot field in OER research, and PBAs have also been a hot topic in direct electrode research due to their strong plasticity. Many researchers have directly prepared different PBA electrodes, such as cubic, array, and thin films, on carriers such as carbon cloth, NF, and stainless steel sheets.[79–81] Here, we prepared NiFe-PBA coated NF (NiFe-PBA@NF) using the method reported in the paper,[81] as shown in Fig. 5a. First, $Ni(OH)_2$ was electrodeposited on the NF and then immersed in $K_3[Fe(CN)_6]$ solution to convert the $Ni(OH)_2$ into NiFe PBA. As clearly observed in Fig. S17, a large number of nano-cubes with typical PBA morphology were grown on the surface of NF. Finally, the target product was obtained through heat treatment. Among them, NiFe-250@NF still retains the basic morphology of NiFe-PBA@NF (Fig. S18).

Benefiting from the direct and intimate connection between NF and catalysts, all PBAs grown directly on NF showed extraordinary performance after heat treatment. Among these derivatives, NiFe-250@NF is especially noteworthy, continuing to demonstrate the most outstanding performance among this group of materials. Specifically, the onset overpotential of NiFe-250@NF is only 190 mV, with a Tafel slope of 39.4 mV dec^{-1}, and the reaction resistance is also the lowest (Fig. 5b–d, S19 and Table S3). More importantly, its performance degradation is minimal after 100 hours of stability testing (Fig. 5e). In order to compare the performance of each electrode more intuitively, the overpotential of all samples at the corresponding current density was plotted as a bar graph in Fig. 5f. Notably, NiFe-250@NF exhibits the most remarkable performance, with overpotentials of 220 mV at 10 mA cm^{-2}, 255 mV at 50 mA cm^{-2}, and 310 mV at 200 mA cm^{-2}, respectively. As observed, NiFe-250@NF has such an excellent anode current density under OER conditions, which will increase the efficiency of the overall electrochemical water-splitting. In addition, NiFe-250 and NiFe-250@NF show excellent electrocatalytic performance for the OER in 1 M KOH with low overpotential at a stable density of 10 mA cm^{-2} and a small Tafel slope, which can be comparable to that of most recently reported PBA derived excellent OER catalysts (Fig. 5g and Table S5).

The outstanding electrode performance of NiFe-250@NF fundamentally originates from the unique intrinsic structural properties of the NiFe-250 material itself. Compared to other reported amorphous NiFe-based catalysts, the distinct advantage of NiFe-250 stems from the structural features imparted by its specific synthesis pathway and the unique reconstruction behavior that follows. Air pyrolysis leads to the decomposition and escape of CN groups from the PBA precursor, a process that likely creates abundant voids or structural defects within the material. This unique mesoscale structure, on the one hand, provides it with the largest electrochemical active surface area, exposing more potential active sites; on the other hand, the open voids significantly facilitate electrolyte infiltration and ion transport, providing a kinetic basis for exceptionally rapid electrochemical activation. More importantly, unlike many amorphous catalysts whose reconstruction depth is often limited, this open architecture that extends throughout the material allows OH^- ions and reactants to penetrate the bulk, enabling NiFe-250 to undergo thorough bulk-phase reconstruction into a homogeneous active NiFeOOH phase. This conclusion is corroborated by multiple lines of evidence: the homogeneous post-OER morphology and the highly consistent elemental ratios between the surface and the bulk. Therefore, the porous amorphous structure induced by CN evolution achieves an ideal integration of rapid kinetics and complete phase transformation. This key material characteristic enables the simultaneous tackling of multiple challenges in OER catalysis: high active-site exposure, fast activation, full bulk utilization, and metal stability.

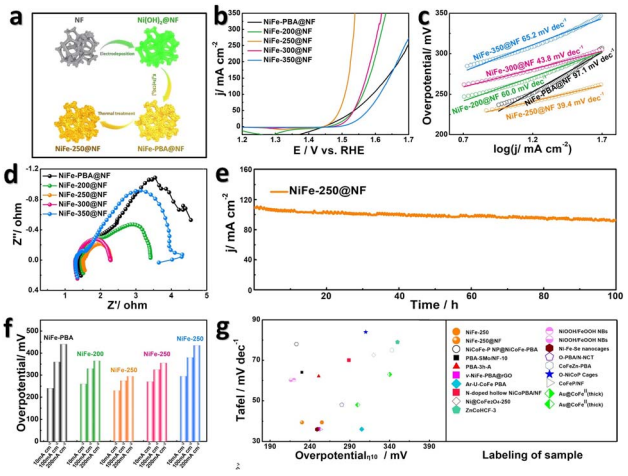

Fig. 5 (a) Schematic illustration showing the preparation route of NiFe-250@NF. (b) LSV, (c) Tafel slopes, (d) Nyquist plots and (e) overpotential data bar chart of NiFe-PBA@NF, NiFe-200@NF, NiFe-250@NF, NiFe-300@NF and NiFe-350@NF. (f) Chronoamperometric tests of NiFe-250 at an overpotential of 300 mV. (g) Comparisons of potential at 10 mA cm^{-2} and Tafel slopes in our studies with those of other excellent PBA derivatives of OER electrocatalysts.

Conclusions

In this study, an amorphous NiFe-250 catalyst with rapid and complete reconstruction characteristics was prepared *via* air pyrolysis of a NiFe-PBA precursor. The amorphous oxide obtained after heat treatment at 250 °C in air demonstrated

excellent OER performance, achieving an overpotential of only 255 mV at a current density of 10 mA cm^{-2} and a Tafel slope of 39.4 mV dec^{-1}. Its performance significantly surpassed that of catalysts containing V_{CN} and crystalline oxide counterparts. The exceptional electrocatalytic properties of this amorphous structure originate from its ultra-fast electrochemical activation, effective stabilization of elemental components, and ability to undergo complete reconstruction into active NiFeOOH. Owing to the general applicability of this method, a NiFe-250@NF electrode was further fabricated through *in situ* growth and thermal treatment on NF. This electrode required only 220 mV overpotential to reach 10 mA cm^{-2} and exhibited stable operation for over 100 hours. This work systematically elucidates the structural evolution of NiFe-PBA during air pyrolysis—from the formation of V_{CN} to amorphous oxide generation and finally to crystallization—along with the corresponding performance trends, providing both experimental evidence and theoretical insight for the rational design of cost-effective, high-performance amorphous catalysts. Furthermore, by thoroughly analyzing the rapid transformation behavior and reconstruction products of the amorphous pre-catalyst during the reaction process, the unique "rapid and complete reconstruction" mechanism was revealed, offering a valuable theoretical foundation for the design of advanced catalytic materials.

Author contributions

Zhen Cao: funding acquisition, investigation, conceptualization, methodology, formal analysis, writing – original draft, project administration. Wenhui Yan: data curation, formal analysis, visualization, investigation, writing – review and editing. Haozhe Shi: data curation, formal analysis, investigation. Tingting Zhou: supervision, data curation, formal analysis, investigation, writing–review and editing. Zhifei Sun: data curation, formal analysis. Yuhan Yang: data curation, formal analysis. Jiali Zhang: data curation. Wenbin Zhang: data curation. Kaili Wang: funding acquisition, project administration, supervision, writing – review and editing.

Conflicts of interest

There are no conflicts to declare.

Data availability

Data supporting this study have been included as part of the main manuscript and supplementary information (SI). Supplementary information: additional data, figures, and methodological details that support the findings presented in the main manuscript. See DOI: https://doi.org/10.1039/d5na00904a.

Acknowledgements

This study was financially supported by the Doctoral Research Foundation of Weifang University (2021BS07) and the Natural Science Foundation of Shandong Province (ZR2025QC566).

References

1 A. G. Olabi and M. A. Abdelkareem, *Renewable Sustainable Energy Rev.*, 2022, **158**, 112111.
2 L. Wu, Y. Xu, Q. Wang, X. Zou, Z. Pan, M. K. H. Leung and L. An, *Energy Environ. Sci.*, 2025, **18**, 4596–4624.
3 X. Zhu, H. Zong, C. J. V. Pérez, H. Miao, W. Sun, Z. Yuan, S. Wang, G. Zeng, H. Xu, Z. Jiang and G. A. Ozin, *Angew. Chem., Int. Ed.*, 2023, **62**, e202218694.
4 Z. Yuan, X. Zhu, X. Gao, C. An, Z. Wang, C. Zuo, D. D. Dionysiou, H. He and Z. Jiang, *Environ. Sci. Ecotechnol.*, 2024, **20**, 100368.
5 E. W. Lees, B. A. W. Mowbray, F. G. L. Parlane and C. P. Berlinguette, *Nat. Rev. Mater.*, 2022, **7**, 55–64.
6 X. Wang, M. Geng, S. Sun, Q. Xiang, S. Dong, K. Dong, Y. Yao, Y. Wang, Y. Yang, Y. Luo, D. Zheng, Q. Liu, J. Hu, Q. Wu, X. Sun and B. Tang, *J. Mater. Chem. A*, 2024, **12**, 634–656.
7 L. Quan, H. Jiang, G. Mei, Y. Sun and B. You, *Chem. Rev.*, 2024, **124**, 3694–3812.
8 H. Hu, X. Wang, J. P. Attfield and M. Yang, *Chem. Soc. Rev.*, 2024, **53**, 163–203.
9 Y. Wang, F. Li, L. Zhao, Y. Wang, G. Yang, J. Tian, S. Heng, X. Sun, J. Zhao, M. Chen and Q. Chen, *Nanoscale*, 2025, **17**, 11101–11132.
10 B.-Y. Zhang, S.-L. Xu, J. Li, H.-Y. Zhou, X. Li, R.-D. Zhao, F.-F. Wu and D. Zhao, *CrystEngComm*, 2025, **27**, 3700–3711.
11 Z. Su, B. Zhang, Y. Wang, X. Li, H. Zhou, Y. Tian, J. Xiang, R.-D. Zhao and L. Miao, *Chem.–Asian J.*, 2025, **20**, e70385.
12 X. Li, S.-l. Xu, J. Li, S.-s. Zhang, B.-y. Zhang, R.-d. Zhao, D.-p. Zhao and F.-f. Wu, *Nanoscale Adv.*, 2025, **7**, 5546–5560.
13 Z. Cao, W. Zhang, T. Zhou, W. Yan and K. Wang, *Molecules*, 2024, **29**, 4562.
14 Q. Wu, Q. Gao, X. Wang, Y. Qi, L. Shen, X. Tai, F. Yang, X. He, Y. Wang, Y. Yao, Y. Ren, Y. Luo, S. Sun, D. Zheng, Q. Liu, S. Alfaifi, X. Sun and B. Tang, *iScience*, 2024, **27**, 108738.
15 X. Lin, J. Xu and Z. Peng, *Next Sustainability*, 2024, **3**, 100023.
16 P. Wang, S. Zhang, Z. Wang, Y. Mo, X. Luo, F. Yang, M. Lv, Z. Li and X. Liu, *J. Mater. Chem. A*, 2023, **11**, 5476–5494.
17 T. Zhou, Z. Liu, B. Yang, Z. Cao, Z. Jiang, W. Cui, K. Wang, L. Yu, J. Lu and L. Zhang, *Front. Chem.*, 2022, **10**, 1047398.
18 Y. Zhou, Z. Wang, M. Cui, H. Wu, Y. Liu, Q. Ou, X. Tian and S. Zhang, *Adv. Funct. Mater.*, 2024, **34**, 2410618.
19 B. M. Hunter, H. B. Gray and A. M. Müller, *Chem. Rev.*, 2016, **116**, 14120–14136.
20 K. Li, Y. Qin, Z.-G. Li, T.-M. Guo, L.-C. An, W. Li, N. Li and X.-H. Bu, *Coord. Chem. Rev.*, 2022, **470**, 214692.
21 Y. Guari, M. Cahu, G. Félix, S. Sene, J. Long, J. Chopineau, J.-M. Devoisselle and J. Larionova, *Coord. Chem. Rev.*, 2022, **461**, 214497.
22 B. Singh and A. Indra, *Mater. Today Energy*, 2020, **16**, 100404.
23 J. Chen, L. Wei, A. Mahmood, Z. Pei, Z. Zhou, X. Chen and Y. Chen, *Energy Storage Mater.*, 2020, **25**, 585–612.
24 L.-M. Cao, D. Lu, D.-C. Zhong and T.-B. Lu, *Coord. Chem. Rev.*, 2020, **407**, 213156.
25 J.-Y. Xie and B. Dong, *Chin. J. Catal.*, 2021, **42**, 1843–1864.

26 H. Xu, L. Yang, K. Wang, L. Jin, Y. Liu, G. He and H. Chen, *Inorg. Chem.*, 2023, **62**, 11271–11277.
27 D. Li, C. Zhou, Y. Xing, X. Shi, W. Ma, L. Li, D. Jiang and W. Shi, *Chem. Commun.*, 2021, **57**, 8158–8161.
28 Z. Cao, T. Zhou, W. Xi and Y. Zhao, *Electrochim. Acta*, 2018, **263**, 576–584.
29 P. Cai, J. Huang, J. Chen and Z. Wen, *Angew. Chem., Int. Ed.*, 2017, **56**, 4858–4861.
30 J. Nai, J. Zhang and X. W. Lou, *Chem*, 2018, **4**, 1967–1982.
31 S. Wang, J. Cai, C. Lv, C. Hu, H. Guan, J. Wang, Y. Shi, J. Song, A. Watanabe and X. Ge, *Chem. Eng. J.*, 2021, **420**, 129972.
32 L. Han, P. Tang, Á. Reyes-Carmona, B. Rodríguez-García, M. Torréns, J. R. Morante, J. Arbiol and J. R. Galan-Mascaros, *J. Am. Chem. Soc.*, 2016, **138**, 16037–16045.
33 X. Su, Y. Wang, J. Zhou, S. Gu, J. Li and S. Zhang, *J. Am. Chem. Soc.*, 2018, **140**, 11286–11292.
34 Y. n. Xia, J. Chi, J. Tang, X. Liu, Z. Xiao, J. Lai and L. Wang, *Chin. J. Catal.*, 2024, **66**, 110–138.
35 T. Zhou, Z. Cao, X. Tai, L. Yu, J. Ouyang, Y. Li and J. Lu, *Polymers*, 2022, **14**, 1510.
36 K. Zhu, F. Shi, X. Zhu and W. Yang, *Nano Energy*, 2020, **73**, 104761.
37 J. Lu, H. Zhang, S. Li, S. Guo, L. Shen, T. Zhou, H. Zhong, L. Wu, Q. Meng and Y. Zhang, *Inorg. Chem.*, 2020, **59**, 3152–3159.
38 Y. Cheng, T. Yu, C. Zheng, X. Lei, J. Li, X. Liu and R. Guo, *Chem. Eng. J.*, 2025, **522**, 167714.
39 C. Wang, P. Shi, C. Guo, R. Guo and J. Qiu, *J. Electroanal. Chem.*, 2024, **956**, 118072.
40 Y. Wu, Y. Li, J. Gao and Q. Zhang, *SusMat*, 2021, **1**, 66–87.
41 R. L. Germscheidt, A. B. S. de Araujo, J. P. B. de Souza, E. Q. Machado, N. S. Galdino, M. A. Z. Arruda, T. C. R. Rocha and J. A. Bonacin, *Electrochim. Acta*, 2025, **529**, 146327.
42 Q. He, L. Han, C. Lin and K. Tao, *Nanoscale*, 2024, **16**, 12368–12379.
43 X. Sun, Y. Fu, R. Chen, H. Lu, Y. Gao, Z. Li, R. Zhang and M. Shao, *Appl. Surf. Sci.*, 2025, **703**, 163399.
44 Z. Xiao, Y.-C. Huang, C.-L. Dong, C. Xie, Z. Liu, S. Du, W. Chen, D. Yan, L. Tao, Z. Shu, G. Zhang, H. Duan, Y. Wang, Y. Zou, R. Chen and S. Wang, *J. Am. Chem. Soc.*, 2020, **142**, 12087–12095.
45 J. Ding, D. Guo, N. Wang, H.-F. Wang, X. Yang, K. Shen, L. Chen and Y. Li, *Angew. Chem., Int. Ed.*, 2023, **62**, e202311909.
46 Z. Cao, H. Shi, T. Zhou, W. Yan, J. Song, P. Feng, K. Wang and Z. Jiang, *Inorganics*, 2025, **13**, 354.
47 S. Jo, J. Kwon, S. Choi, T. Lu, Y. Byeun, H. Han and T. Song, *Appl. Surf. Sci.*, 2022, **574**, 151620.
48 F. Diao, M. Rykær Kraglund, H. Cao, X. Yan, P. Liu, C. Engelbrekt and X. Xiao, *J. Energy Chem.*, 2023, **78**, 476–486.
49 Q. Ruan, D. Li, C. Wu, C. Huang and P. K. Chu, *EcoEnergy*, 2024, **2**, 268–277.
50 Z.-Y. Yu, Y. Duan, J.-D. Liu, Y. Chen, X.-K. Liu, W. Liu, T. Ma, Y. Li, X.-S. Zheng, T. Yao, M.-R. Gao, J.-F. Zhu, B.-J. Ye and S.-H. Yu, *Nat. Commun.*, 2019, **10**, 2799.
51 J. Wang, M. Li, Y. Zhai, F. Wang, X. Zhang, H. Lv, T. Yu and W. Zhang, *Appl. Surf. Sci.*, 2021, **556**, 149789.
52 F. Guo, Y. Zhang, L. Cai and L. Li, *Composites, Part B*, 2022, **233**, 109650.
53 M. Khairy, K. G. Mahmoud and H. M. El-Sagher, *Int. J. Hydrogen Energy*, 2023, **48**, 29887–29897.
54 W.-B. Wang, H.-J. Cao and G.-L. Li, *Inorg. Chem.*, 2023, **62**, 10241–10248.
55 M. Jiang, X. Fan, S. Cao, Z. Wang, Z. Yang and W. Zhang, *J. Mater. Chem. A*, 2021, **9**, 12734–12745.
56 G. Liu, X. Gao, K. Wang, D. He and J. Li, *Int. J. Hydrogen Energy*, 2016, **41**, 17976–17986.
57 G. Liu, K. Wang, X. Gao, D. He and J. Li, *Electrochim. Acta*, 2016, **211**, 871–878.
58 Z. Cao, T. Zhou, X. Ma, Y. Shen, Q. Deng, W. Zhang and Y. Zhao, *ACS Sustainable Chem. Eng.*, 2020, **8**, 11007–11015.
59 J. Qiao, F. Song, J. Hu, D. Huo, J. Yuan, J. Shen, L. Niu and A.-j. Wang, *Int. J. Hydrogen Energy*, 2019, **44**, 16368–16377.
60 S. Pal, S. Jana, D. K. Singh, V. Ganesan, U. P. Azad and R. Prakash, *Int. J. Hydrogen Energy*, 2024, **50**, 52–65.
61 Y. Hao, G. Du, Y. Fan, L. Jia, D. Han, W. Zhao, Q. Su and B. Xu, *Appl. Surf. Sci.*, 2023, **614**, 156237.
62 F. Zhang, Y. Shi, T. Xue, J. Zhang, Y. Liang and B. Zhang, *Sci. China Mater.*, 2017, **60**, 324–334.
63 Z. Wu, Z. Zou, J. Huang and F. Gao, *J. Catal.*, 2018, **358**, 243–252.
64 L. Qiu, Q. Wang, P. Yan and X.-Y. Yu, *J. Mater. Chem. A*, 2022, **10**, 21251–21259.
65 C. Zhang, J. Chen, J. Zhang, Y. Luo, Y. Chen, Y. Xue, Y. Yan, Y. Jiao, G. Wang and R. Wang, *J. Colloid Interface Sci.*, 2022, **607**, 967–977.
66 Y. Guo, T. Wang, J. Chen, J. Zheng, X. Li and K. Ostrikov, *Adv. Energy Mater.*, 2018, **8**, 1800085.
67 Z. Cao, T. Zhou, X. Ma, Y. Shen, Q. Deng, W. Zhang and Y. Zhao, *ACS Sustainable Chem. Eng.*, 2020, **8**, 11007–11015.
68 K. Wang, Y. Xu, V. Daneshvariesfahlan, M. Rafique, Q. Fu, H. Wei, Y. Zhang, J. Zhang, B. Zhang and B. Song, *Nanoscale*, 2025, **17**, 6287–6307.
69 A. Ibrahim, M. Shiraishi, Z. Homonnay, S. Krehula, M. Marciuš, A. Bafti, L. Pavić and S. Kubuki, *Int. J. Mol. Sci.*, 2023, **24**, 14300.
70 H. Ding, H. Liu, W. Chu, C. Wu and Y. Xie, *Chem. Rev.*, 2021, **121**, 13174–13212.
71 M. B. Stevens, C. D. M. Trang, L. J. Enman, J. Deng and S. W. Boettcher, *J. Am. Chem. Soc.*, 2017, **139**, 11361–11364.
72 H. S. Ahn and A. J. Bard, *J. Am. Chem. Soc.*, 2016, **138**, 313–318.
73 J. Y. C. Chen, L. Dang, H. Liang, W. Bi, J. B. Gerken, S. Jin, E. E. Alp and S. S. Stahl, *J. Am. Chem. Soc.*, 2015, **137**, 15090–15093.
74 L. Trotochaud, S. L. Young, J. K. Ranney and S. W. Boettcher, *J. Am. Chem. Soc.*, 2014, **136**, 6744–6753.
75 D. Wu, L. Hu, X. Liu, T. Liu, X. Zhu, Q. Luo, H. Zhang, L. Cao, J. Yang, Z. Jiang and T. Yao, *Nat. Commun.*, 2025, **16**, 726.

76 H. Xiao, H. Shin and W. A. Goddard, *Proc. Natl. Acad. Sci. U. S. A.*, 2018, **115**, 5872–5877.
77 Y. Lin, H. Ren, S. Zhang, S. Liu, T. Zhao, W.-J. Jiang, W. Zhou, J.-S. Hu and Z. Li, *Adv. Energy Mater.*, 2024, **14**, 2302403.
78 X. Liu, K. Ni, B. Wen, R. Guo, C. Niu, J. Meng, Q. Li, P. Wu, Y. Zhu, X. Wu and L. Mai, *ACS Energy Lett.*, 2019, **4**, 2585–2592.
79 L.-M. Cao, Y.-W. Hu, D.-C. Zhong and T.-B. Lu, *ChemSusChem*, 2018, **11**, 3708–3713.
80 X. Xu, T. Wang, L. Su, Y. Zhang, L. Dong and X. Miao, *ACS Sustainable Chem. Eng.*, 2021, **9**, 5693–5704.
81 Y. Wang, J. Ma, J. Wang, S. Chen, H. Wang and J. Zhang, *Adv. Energy Mater.*, 2019, **9**, 1802939.